Journal of Structural Geology 31 (2009) 1395–1408

Contents lists available at ScienceDirect

Journal of Structural Geology

journal homepage: www.elsevier.com/locate/jsg

'Diffuse faulting' in the Machu Picchu granitoid pluton, Eastern Cordillera, Peru

Stefano Mazzoli [a,*], Stefano Vitale [a], Giuseppe Delmonaco [b], Vincenzo Guerriero [a], Claudio Margottini [b], Daniele Spizzichino [b]

[a] Dipartimento di Scienze della Terra, Università di Napoli 'Federico II', Largo San Marcellino 10, 80138 Napoli, Italy
[b] ISPRA – Istituto per la Protezione e la Ricerca Ambientale, Servizio Geologico d'Italia, Dipartimento Difesa del Suolo, Via Curtatone 3, 00185 Roma, Italy

ARTICLE INFO

Article history:
Received 14 January 2009
Received in revised form
3 August 2009
Accepted 9 August 2009
Available online 14 August 2009

Keywords:
Fracture analysis
Structural inheritance
Strain localization
Distributed deformation
Central Andes

ABSTRACT

A series of batholiths, forming part of the 'roots' of a Permo-Liassic rift system, are exposed in the high Eastern Cordillera of central Peru as a result of tectonic inversion. Shortening of the Machu Picchu granitoid pluton was accommodated by widespread shear reactivation of primary joints, by a process termed here 'diffuse faulting'. Fault-like reactivation of precursor joint surfaces, marked by chlorite, epidote and quartz shear fibres, is locally evidenced by few centimetres offsets within apparently undeformed granite. Analysis of fault slip data indicates that shear reactivation of different joint sets was kinematically consistent with ENE oriented shortening. Less frequent mylonitic shear zones appear to have evolved from the common brittle precursors. Apart from rare phyllonitic shear zones, fluid–rock interaction along the brittle precursors was generally limited, and pluton deformation appears to be mainly controlled by the geometry and distribution of primary joints. Three main sets of reactivated joints can be recognized, characterized by oblique-slip kinematics with variable reverse and strike–slip components of motion. Theoretical modelling based on quantitative fracture analysis (scan-line data) and different displacement–length relationships applied to the main reactivated joint sets yield first-order estimates of pluton finite strain. The results suggest that bulk finite strain is oblate and essentially coaxial, and is characterized by horizontal shortening not exceeding 10%. Relatively small finite strains, integrated over the size of the pluton, still result in a few kilometres of crustal shortening.

1. Introduction

In the last twenty years, the process of basin inversion has received considerable attention. Numerous studies integrating basin stratigraphy, structural analysis and/or analogue and numerical modelling allowed geoscientists to obtain a progressively better understanding of the geometry, modes and mechanisms of basin inversion (e.g. Cooper and Williams, 1993; Buchanan and Buchanan, 1995; Glen et al., 2005 and references therein). However, little is known about the deformation occurring at depth, in the 'roots' of rift basins – often occupied by magmatic complexes – during tectonic inversion. In the Eastern Cordillera of southern Peru, granitoid plutons originally emplaced along a Permo-Liassic rift axis are presently exposed at high elevations as a result of strong inversion of the axial zone of the rift system (Sempere et al., 2002). This provides a unique opportunity to analyze the effects of Andean shortening and basin inversion in homogenous rock bodies originally sitting in the 'roots' of the rift system.

It is well known that, in homogeneous plutonic rocks, strain tends to be partitioned and is mainly localized along shear zones. Since the pioneering work of Ramsay and Graham (1970), these represent widely investigated, 'classic' geological structures (e.g. Vitale and Mazzoli, 2008, 2009 and references therein). A broad literature exists on rheology-dependent strain localization in homogenous plutonic rocks. In particular, the role of fluids and chemical softening has been intensely investigated (e.g. Christiansen and Pollard, 1997; Tourigny and Tremblay, 1997), as well as the fundamental control exerted by brittle precursor structures in shear zone nucleation; the interested reader is referred to the papers by Pennacchioni (2005), Mancktelow and Pennacchioni (2005) and Pennacchioni and Mancktelow (2007) for exhaustive reviews and critical discussions of these issues.

Structural analysis of the Machu Picchu granitoid pluton, being characterized by pre-existing, well-developed planar discontinuities at the time of low-T deformation, confirms the fundamental role played by structural inheritance and brittle fracture reactivation in shear zone nucleation. Furthermore, this study attempts

* Corresponding author.
E-mail address: stefano.mazzoli@unina.it (S. Mazzoli).

0191-8141/$ – see front matter © 2009 Elsevier Ltd. All rights reserved.
doi:10.1016/j.jsg.2009.08.010

to obtain an estimate of bulk finite strain and crustal shortening associated with joint reactivation within a large pluton located at the base of the upper crust at the time of basin inversion. The aim is to provide new, quantitative insights into the modes of deformation of common continental crust rock bodies such as plutonic complexes involved in crustal shortening. Our results may hopefully also contribute to the more general debate on the roles of localized (non-coaxial) vs. distributed (and essentially coaxial) deformation in convergent tectonic settings (e.g. Butler and Mazzoli, 2006).

2. Geological setting

The Andean chain represents the paradigm of continental orogeny resulting from the subduction of an oceanic slab beneath a continental plate (e.g. Ramos and Aleman, 2000 and references therein). The chain is classically divided into three main sectors (Jaillard et al., 2002): (i) a forearc zone, including the Pacific slope and offshore areas; (ii) an arc zone, mainly represented by the present chain (and the Altiplano); and (iii) a back-arc area, which includes the Eastern Cordilleras and Amazonian slope and foothills and the eastern lowlands underlain by the foreland basin. Since the Tertiary, each zone is dominated by distinctive deformation styles.

Extension-related, tectonic and magmatic manifestations affected the Andean margin (Eastern Cordillera) of Peru and Bolivia between Permian and Jurassic times. According to Sempere et al. (2002) this rift structure controlled the location and nature of subsequent contractional deformation and allowed the individualization of crustal blocks characterized by distinct tectonic behaviour and evolution. The Machu Picchu granitoid pluton, forming part of the larger 'Quillabamba granite' (a magmatic complex exposed in the high Eastern Cordillera of central Peru NW of Cusco; Fig. 1), is one of a series of plutons intruded along the axial zone of such Permo-Liassic rift system. Available geochronological (U–Pb) data provide an age of 257 ± 3 Ma for the Quillabamba granite (Lancelot et al., 1978), whereas Andean convergent deformation affected the study area mainly in Eocene times ('Inca 1 tectonic event', which took place at 43–40 Ma according to Carlotto, 2002), although an early, weak tectonic inversion episode may have occurred already in latest Jurassic–earliest Cretaceous times (Sempere et al., 2002). Shortening produced strong tectonic inversion of the axial zone of the rift system. As a result, the granitoid plutons forming part of the rift 'roots' are now exposed at the highest altitudes (Sempere et al., 2002) allowing studying the effects, on these bodies, of the deformation associated with rift-scale tectonic inversion.

The Machu Picchu granitoid pluton includes a variety of rock types, dominantly granites and granodiorites (Carlotto et al., 1996). The main plutonic body is a medium-grained (millimetre grain size), rather equigranular granite to granodiorite composed of quartz, plagioclase, biotite, K-feldspar ± muscovite. It includes enclaves of more basic composition, being also crosscut by planar

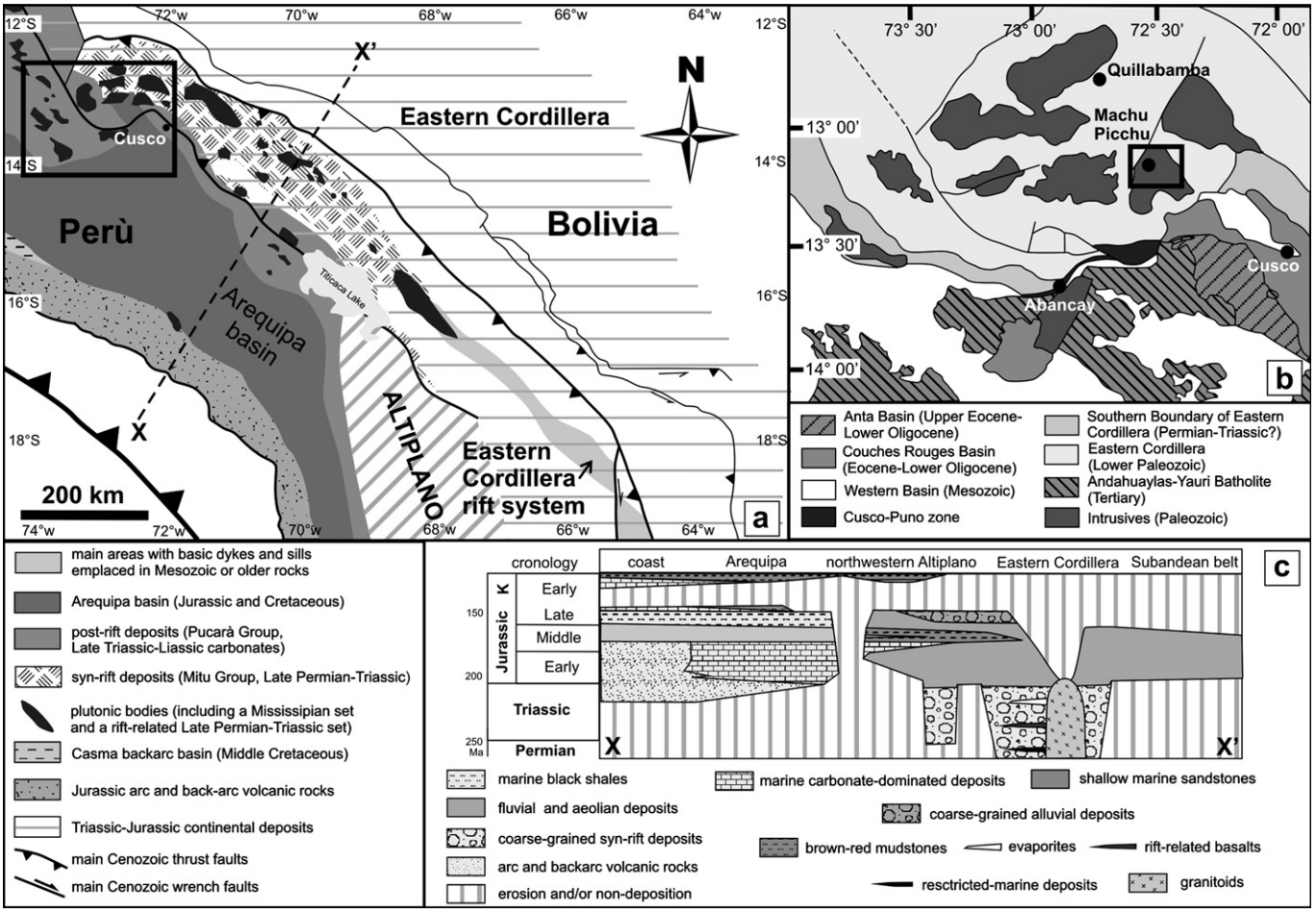

Fig. 1. (a) Geological sketch map showing main Mesozoic elements of Peru and Bolivia (after Sempere et al., 2002). (b) Geological sketch map of the Cusco–Abancay area (after Carlotto, 2002), showing location of field study area. (c) Schematic stratigraphic transect (located in a) showing position of Permo-Triassic plutons of the Eastern Cordillera (after Sempere et al., 2002).

Fig. 2. Plutonic rocks and joint sets. (a) Primary relationships among igneous rocks of different composition. (b) Microphotograph (crossed polars) of undeformed granite (note plagioclase alteration, and quartz microstructures including undulose extinction, incipient grain boundary migration and subgrain development at grain margins). (c) Steeply SW-dipping (Set 1) and moderately NE-dipping (Set 3) master joints. (d) Set 3 master joints and steeply NE-dipping secondary joints. (e) Detail of Set 3 joints, showing variable fracture spacing at the outcrop scale. (f) NE-trending, vertical (Set 2) master joints intersecting Set 1 and Set 3 master joints.

intrusions consisting of porphyritic biotite-bearing lamprophyres and aplitic dykes. The batholith, presently preserving intrusive contacts with surrounding Lower Paleozoic pre-rift successions, shows a general rounded shape in map view, with an average diameter of *ca*. 30 km (Carlotto et al., 1996).

3. Structural analysis

Most of the plutonic body shows little macroscopic evidence of deformation and metamorphism, igneous relationships being well preserved (Fig. 2a). Although the igneous fabric is macroscopically well preserved, in thin section (Fig. 2b) many investigated samples display deformation microstructures and a variable low-T metamorphic overprint of the primary minerals. Typical is the alteration and replacement of plagioclase by epidote–sericite–calcite assemblages, pervasively distributed within grains and/or concentrated along plagioclase cleavage planes and intragranular fractures, as well as the replacement of biotite by chlorite.

The most evident structures at the outcrop scale consist of planar joint sets (Fig. 2c–f) that, as discussed in the following sections, may be variably reactivated. The origin of these joint sets, being it related to thermal and/or tectonic stresses acting during cooling of the main plutonic body, is not a subject of this paper. What is important in this context is that batholiths are commonly characterized by variably oriented sets of primary joints (as we shall term them throughout this paper), which form typical networks of planar discontinuities within plutonic bodies (e.g. Price and Cosgrove, 1990). Orientation data for these structures, measured in the Machu Picchu pluton, are shown in Fig. 3.

3.1. Joints

Granitoid rocks showing no evidence of solid-state deformation at the outcrop scale are commonly crosscut by isolated joints of variable length, the larger of which (master joints) may extend for several tens of metres (Fig. 2c–f). These fractures are segmented and show en-echelon geometry, usually with a slight overlap at

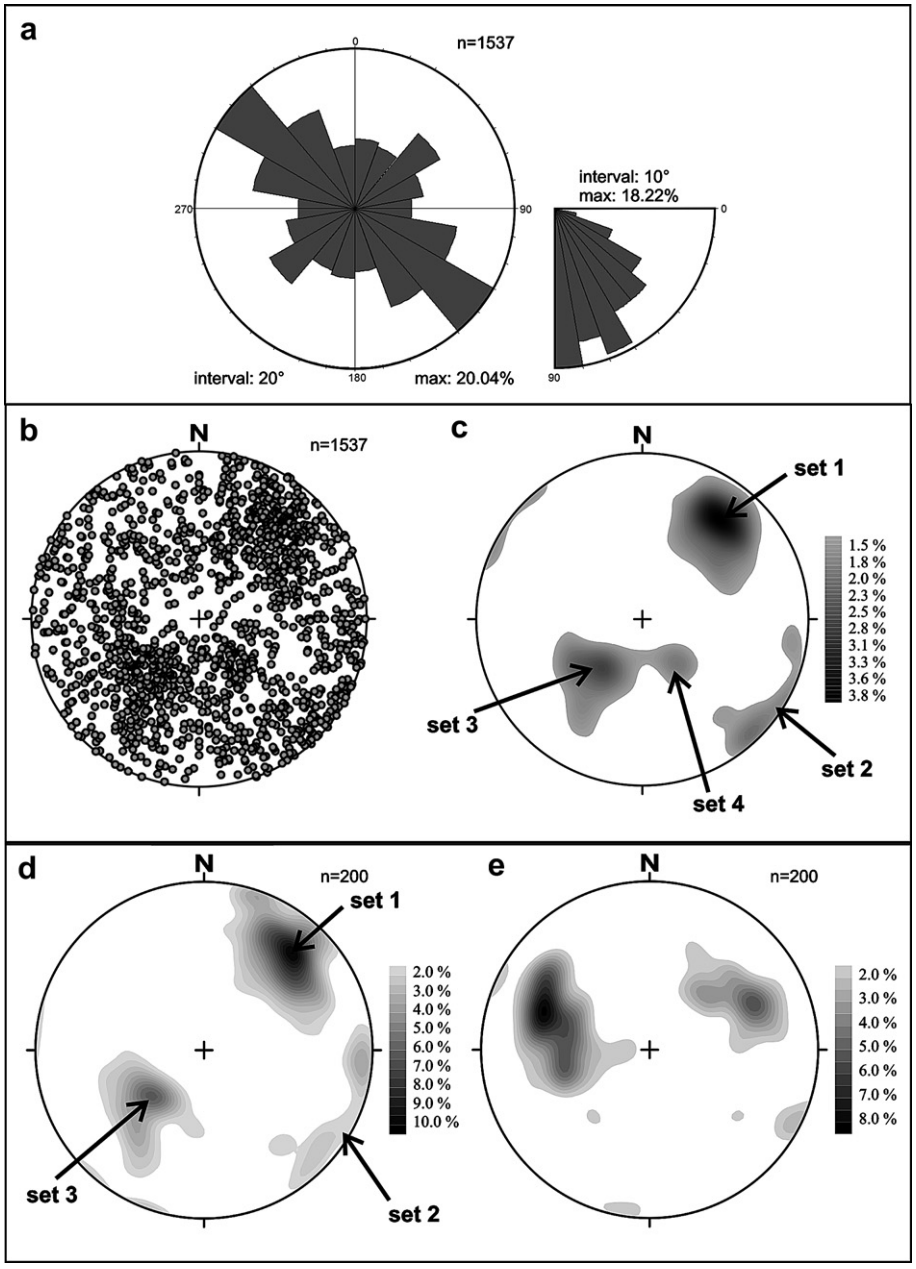

Fig. 3. Orientation data (b–e are lower hemisphere, equal area projections). (a) Rose diagram for all measured planar structures. (b) Poles to planes (all measured structures). (c) Contour plot of data shown in (b); main joint sets are labelled as in text. (d) Contour plot of poles to shear planes. (e) Contour plot of striae/shear fibre lineation data.

their terminations. They generally show no evidence of cataclasis and also little or no alteration by fluid–rock interaction (in fact the typical bleached haloes are uncommon here). The joints show variable spacing, from several centimetres to few metres, and a wide range of attitudes (Fig. 3a). However, four dominant sets can be recognized (Fig. 3b). These, also coinciding with the master joint sets, include: (i) a steeply SW-dipping set; (ii) a N to NE-trending, vertical set; (iii) a moderately NE-dipping set; and (iv) a gently NW dipping set. In the following, they will be indicated as Set 1, Set 2, Set 3, and Set 4, respectively.

Rare mafic dykes occur, parallel to the main joint systems (Fig. 4a). This feature suggests that the joints formed early, most probably during cooling of the main plutonic body, and were intruded by late-magmatic dykes. The lamprophyres also show evidence of lower greenschist facies metamorphism. Fluid influx is suggested by intense low-T overprinting, with widespread replacement of biotite by chlorite (Fig. 4b). Mafic dykes also display common evidence of shear along the contact with wall-rock granite, testified by surfaces coated with mineral shear fibres and local development of gouge bands (Fig. 4c).

3.2. Brittle shear zones

Planar structures forming part of the joint sets described in the previous section (Fig. 3) may show evidence of fault-like reactivation, marked by chlorite, epidote and quartz shear fibres (Fig. 4d and e). Fault offsets cannot usually be obtained, due to the general lack of suitable markers. However, displacements can sometimes be measured at the intersection between different reactivated joint sets within apparently undeformed granite. Such

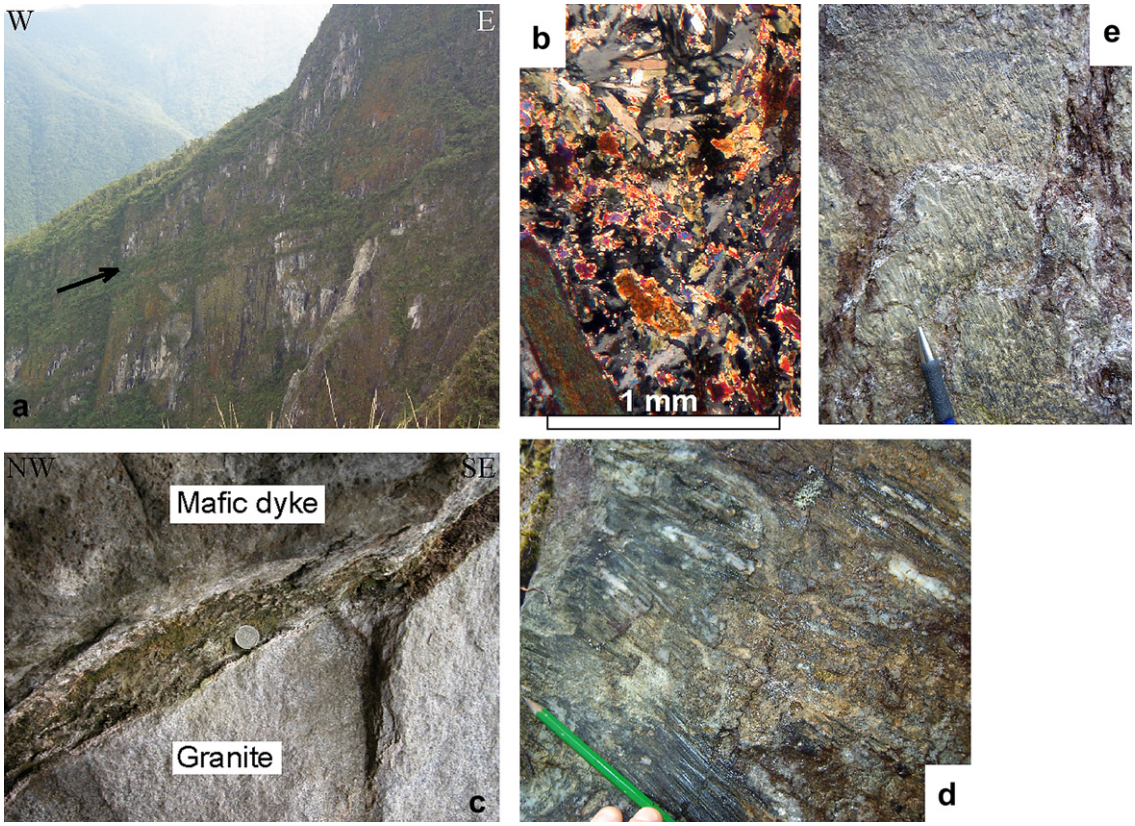

Fig. 4. (a) Mafic dyke (arrowed) intruded parallel to primary joints at Huayna Picchu Mt. (b) Thin section view (crossed polars) of lamprophyre, showing composition dominated by feldspars and biotite (largely replaced by chlorite as a result of low-T metamorphic overprint). (c) Fault gouge (brown) along the contact between lamprophyre and wall-rock granite. (d) Reactivated joint surface showing quartz shear fibres and chlorite. (e) Reactivated joint surface showing epidote shear fibres. (For interpretation of the references to colour in this figure legend, the reader is referred to the web version of this article.)

joint intersections provide relevant information. For example, in Fig. 5a NE-dipping (Set 3) fractures are shown, offsetting a steep SW-dipping (Set 1) surface, producing a series of steps associated with the reverse component of motion of Set 3 fractures. However, the stepped surface also appears to have been reactivated, the steps tending to be smoothed out by oblique shearing along the steep SW-dipping surface (Fig. 5b). These features suggest that: (i) the different fracture sets were reactivated more or less synchronously, during a shortening event; and (ii) the displacements were small (of a few centimetres), so that slip along a reactivated joint set produced asperities that could be smoothed out by shearing along another set at a high angle to the first one.

A straight foliation is sometimes developed at an angle of *ca.* 45° to the reactivated joint, extending for a few centimetres into the adjacent country rock (Fig. 5c), particularly at compressive jogs between stepped terminations of en-echelon fractures. The fact that the foliation is straight and at *ca.* 45° to the bounding reactivated joint segments confirms that the shear displacement is generally small, leading to a correspondingly low finite strain within the compressive bridges, as discussed in Mancktelow and Pennacchioni (2005). According to the latter Authors, the displacement rates on the reactivated joints must have been sufficiently low for strain to be accommodated within the jog zones in a distributed fashion and local cleavage development.

Away from compressive jogs, the wall rock to fault-like reactivated joints generally consists of apparently undeformed granite, macroscopically showing no evidence of alteration by fluid–rock interaction. In thin section, wall-rock granite shows no major differences, in terms of alteration and fabric development, with respect to country rock granite (Fig. 5d). Only in a sub-millimetre thick zone in contact with the fault plane, the breakdown of plagioclase and of iron–magnesium-bearing minerals becomes more intense (Fig. 5e and f). This appears to represent an incipient stage of reaction softening and development of phyllosilicate-rich assemblages that are important for the next group of structures.

3.3. Mylonitic shear zones

Mylonitic shear zones consist of several centimetres to tens of centimetres thick bands of sigmoidally shaped foliation, typical of heterogeneous ductile shear zones, flanking the brittle precursor fracture (Fig. 6a). The latter also shows clear evidence of slip, in the form of mineral shear fibres, consistent with shear zone kinematics. Ductile bands show a mylonitic fabric, including typical S-C structures and shear bands (Fig. 6b), and dynamic recrystallization of quartz dominated by subgrain rotation recrystallization (Fig. 6c).

Several tens of centimetres thick phyllonites also occur within the study area, although they are rare, representing $<1\%$ of the reactivated joints. They show a mylonitic fabric and replacement of the original mineral assemblage of the granite, dominated by quartz and plagioclase, by one consisting of quartz, epidote–sericite and chlorite (Fig. 6d). These phyllonitic levels appear to represent more evolved shear zones that nucleated along the common brittle precursors, but underwent more intense reaction softening, allowing strain localization.

3.4. Brittle shear zone kinematics and paleostress analysis

Three out of four main sets characterizing the whole joint population have been preferentially reactivated (Fig. 3). Set 1

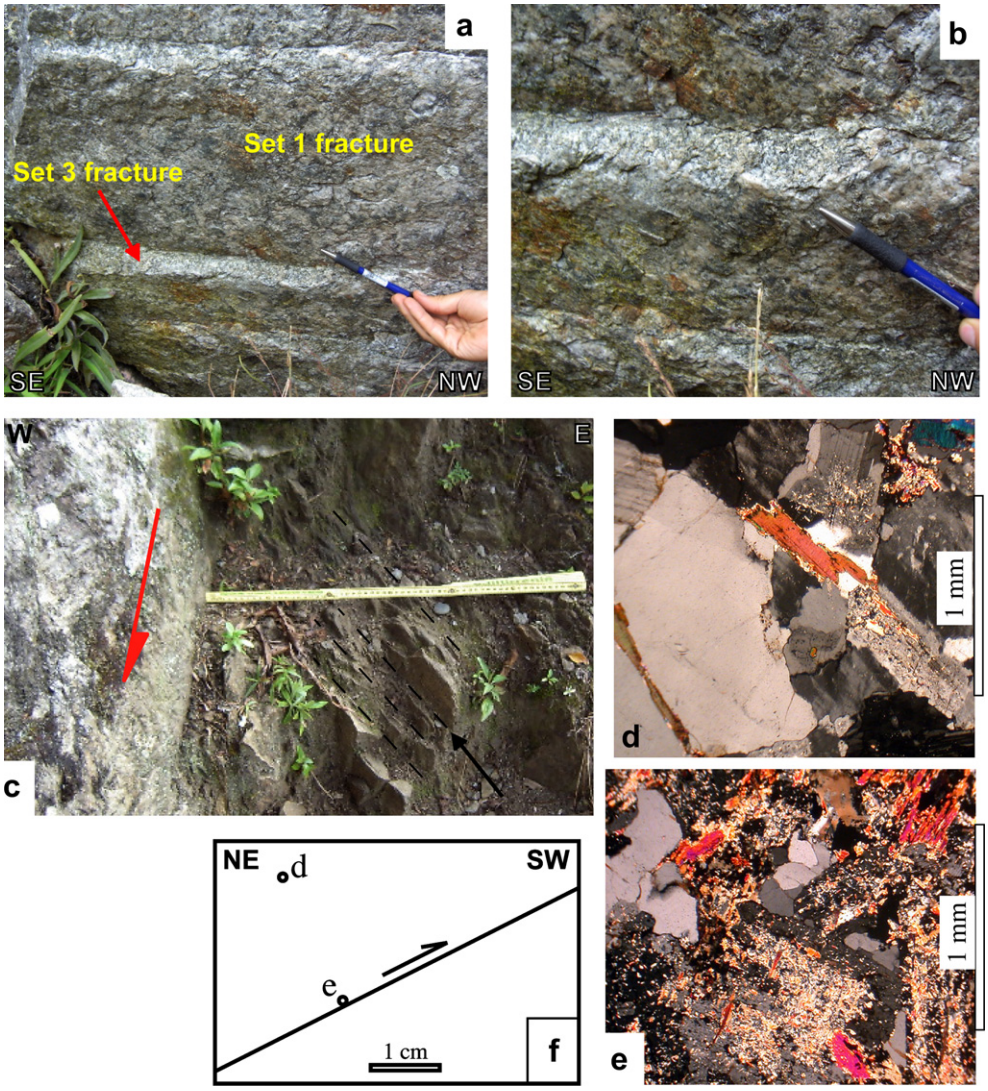

Fig. 5. Brittle shear zones. (a) Stepped surface developed at the intersection between two reactivated joint sets. (b) Detail of previous picture, showing steps (produced by the reverse component of motion along NE-dipping, Set 3 fractures) being smoothed out by oblique shearing along the steep SW-dipping surface. (c) Straight foliation (arrowed) at dextral strike–slip fault termination (reactivated, NNE striking, Set 2 joint; large arrow to the left shows strike–slip motion). (d) Thin section view (crossed polars) of hanging-wall granite 2 cm away from NE-dipping, reactivated Set 3 joint surface. (e) Thin section view (crossed polars) of hanging-wall granite in contact with reactivated Set 3 joint surface. Note intense plagioclase alteration and breakdown of biotite. (f) Sketch showing location of previous thin sections with respect to NE-dipping, Set 3 joint reactivated as oblique-slip fault with a dominant reverse component of motion.

(steeply SW-dipping) joints and Set 3 (moderately NE-dipping) joints are generally reactivated as reverse-sinistral, oblique-slip faults (the reverse component being dominant for Set 3), whereas Set 2 (vertical, N to NE trending) joints are characterized by dextral strike–slip (Fig. 7). These three joint sets appear to have acted as independent slip systems during convergent deformation (Fig. 8).

Two methods have been used for paleostress analysis, and the results compared (Fig. 9). The right dihedra method (Angelier and Mechler, 1977) provides the following attitudes for the principal stress axes: $\sigma_1 = 246/07$; $\sigma_2 = 155/12$; $\sigma_3 = 008/76$. A second method involves estimating the orientation of the principal stress axes (or *P*-*B*-*T* axes; Turner, 1953) using a value of Θ (angle between the shear plane and the *P* axis, i.e. σ_1) defined by the maximum clustering of *P* and *T* axes (Wallbrecher, 1986). In our instance, a Θ value of 50° is obtained. The contour plots indicate a well-defined *P* axis showing an ENE–WSW horizontal compression, consistent with the σ_1 axis obtained by the right dihedral method. On the other hand, the *B* and *T* axes tend to be more distributed along a great circle (σ_2–σ_3 plane).

The lack of reactivation of Set 4 joints is most probably controlled by their orientation, as these fractures are striking roughly parallel to the maximum compression direction (i.e. they experienced only minor or no shear stress). It is worth noting that, on the contrary, joint Sets 1–3 are suitably oriented for reactivation, the maximum compression direction forming an angle close to 50° with respect to all three joint set mean planes (therefore, the $\sigma 1$ axis approaches the bisector of the trihedral angle formed by the three quasi-orthogonal joint sets).

3.5. Fracture analysis (scan-line data) for the main reactivated joint sets

The basic structure detection technique used for quantitative fracture analysis consisted of measuring fractures along linear traverses (scan lines). Eighteen scan lines were carried out, their length ranging between 5 and 20 m. The following characteristics have been recorded for each detected planar feature: (i) type (joint, reactivated joint, vein, dyke), (ii) distance from scan-line origin,

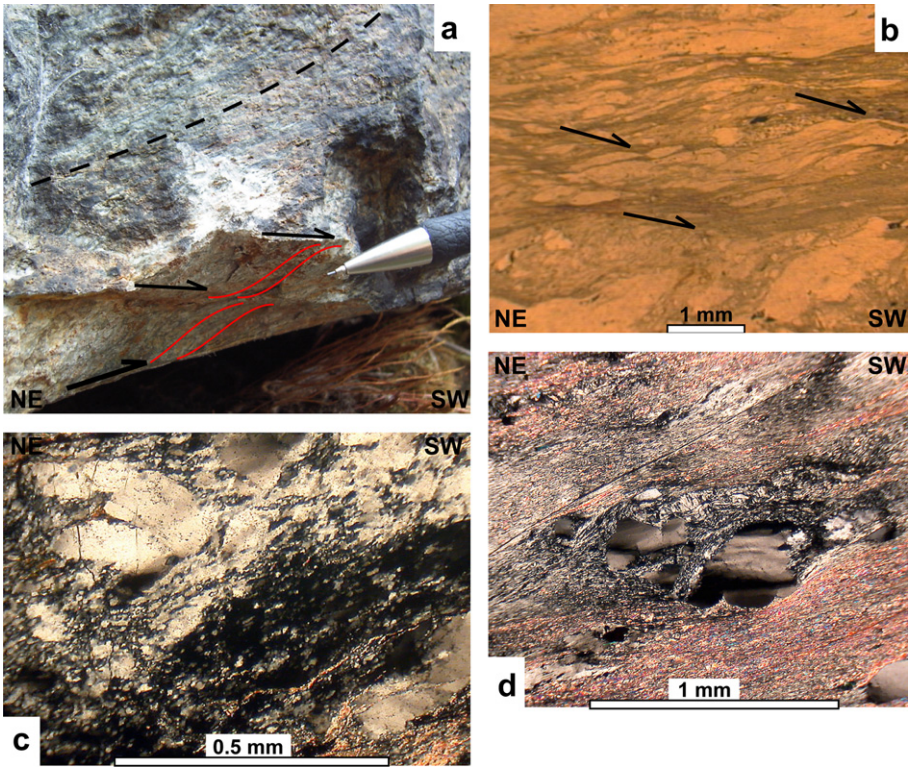

Fig. 6. Mylonitic shear zones developed along NE dipping, Set 3 brittle precursors (sense of shear is top-to-the-SW for all diagrams). (a) Heterogeneous ductile shear zone, showing sigmoidally shaped foliation (hatched line) and shear bands (thin arrows; note deflected foliation along shear bands), flanking reactivated (thick arrow) primary joint surface. (b) Thin section view of mylonite showing shear bands. (c) Thin section view (crossed polars) of mylonite showing sigmoidally shaped foliation and dynamic recrystallization of quartz (dominated by subgrain rotation recrystallization). (d) Thin section view (crossed polars) of phyllonite. The mineral assemblage is dominated by quartz, sericite, fine-grained epidote and chlorite.

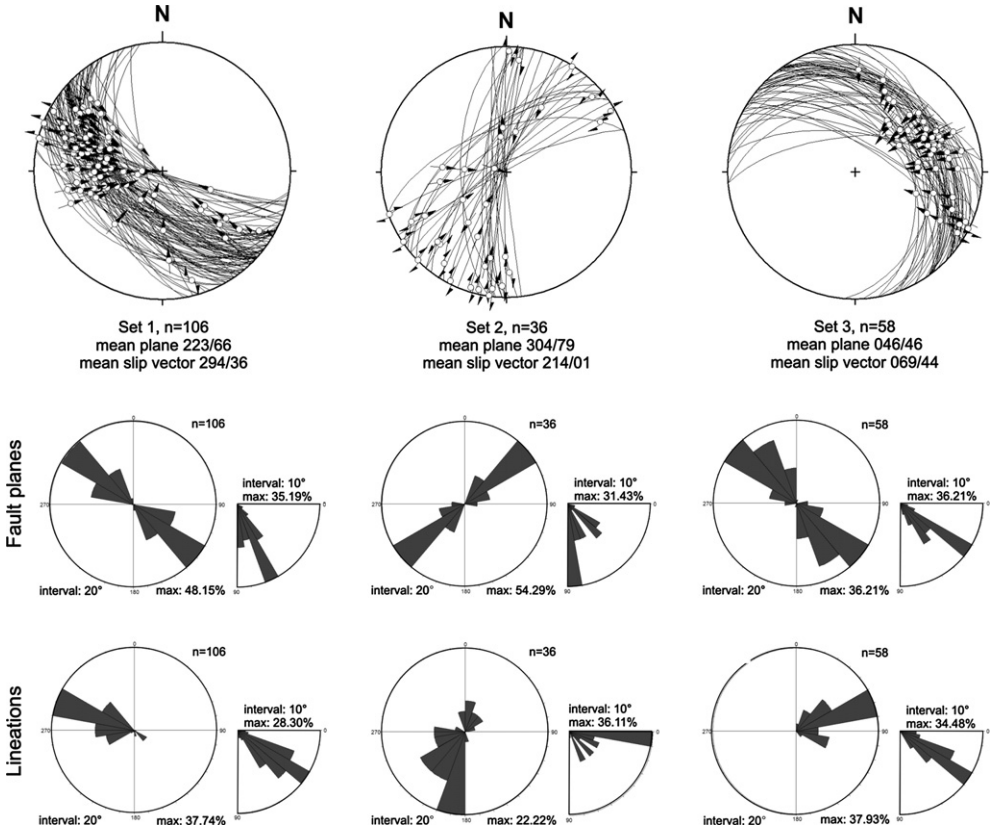

Fig. 7. Orientation data for the three main brittle shear zone sets (reactivated joints). In the upper row (lower hemisphere, equal area projections), fault planes are plotted as great circles, with striae/shear fibre lineation on shear surfaces. Rose diagrams refer to fault planes (medium row) and lineation data (lower row).

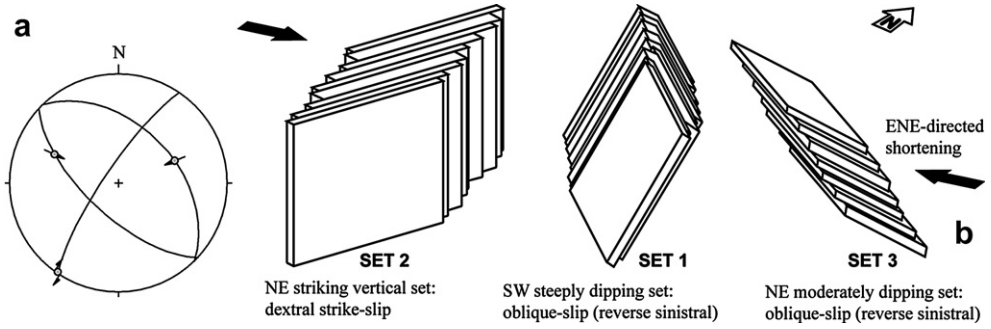

Fig. 8. The three main brittle shear zone sets. (a) Mean slip planes and associated slip vectors (based on orientation data in Fig. 7). (b) Cartoon showing reactivation pattern.

(iii) attitude, (iv) length, (v) aperture (or opening displacement), (vi) shear displacement (when measurable), (vii) morphology, (viii) crosscutting relationships, (ix) composition and texture of fracture fill. As the purpose of the present study is to analyze the role of reactivated primary fractures in pluton deformation, only the results concerning the joints belonging to the three main reactivated families (i.e. Sets 1–3) will be presented.

In order to obtain correct fracture density estimates, for each of the three main reactivated fracture sets the data have been projected onto a section normal to the mean joint plane. The ratio (r) between the standard deviation and the mean of spacing values is of 0.84, 0.55 and 0.50 for joint Sets 1, 2, and 3, respectively. Values of $r < 1$ point out a clustered spatial distribution of joints (Gillespie et al., 1993): compared with a random distribution (characterized by $r = 1$), 'small' and 'large' spacing values are more frequent with respect to the mean. Fig. 10a and b shows the cumulative distributions of spacing values and related best-fit diagrams. The latter display the standard normal distribution inverse function of observed cumulative distributions as a function of spacing (S). Using these diagrams allows one verifying whether an analyzed aleatoric variable (AV) is characterized by a normal or log-normal distribution and, in the latter instance, to obtain the equation of the

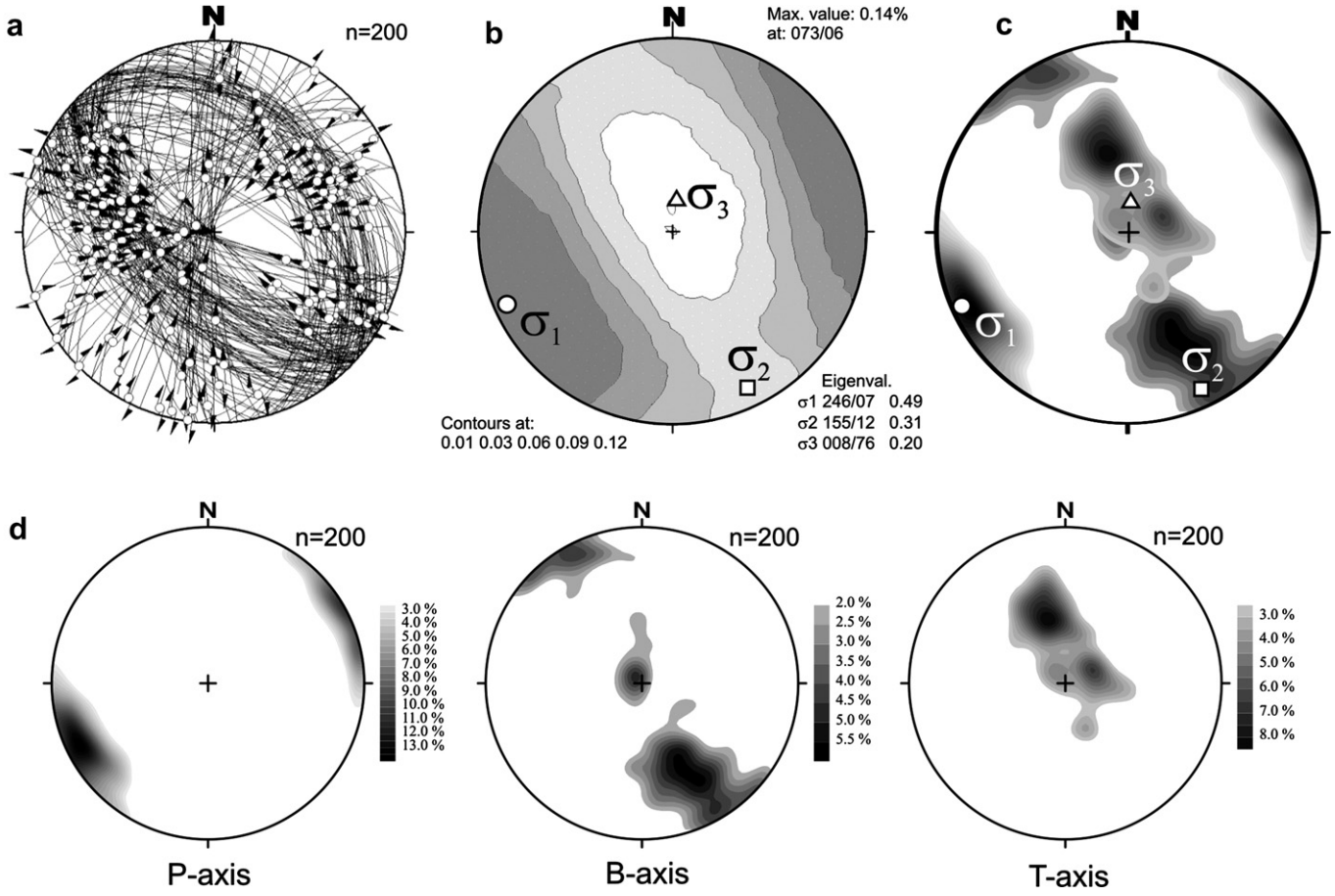

Fig. 9. (a) Plot of all fault planes (including the three sets of Fig. 7), showing striae/shear fibre lineation on shear surfaces. (b) Results of paleostress analysis for faults in (a), carried out using the right dihedra method (Angelier and Mechler, 1977). (c) Contour plot of *P-B-T* distribution, showing orientation of σ_1, σ_2 and σ_3 determined by the right dihedra method for comparison. (d) Contour plots of *P*, *B* and *T* axes separate distributions. Plots and paleostress analysis were performed using TectonicsFP (software by F. Reiter and P. Acs for Microsoft Windows).

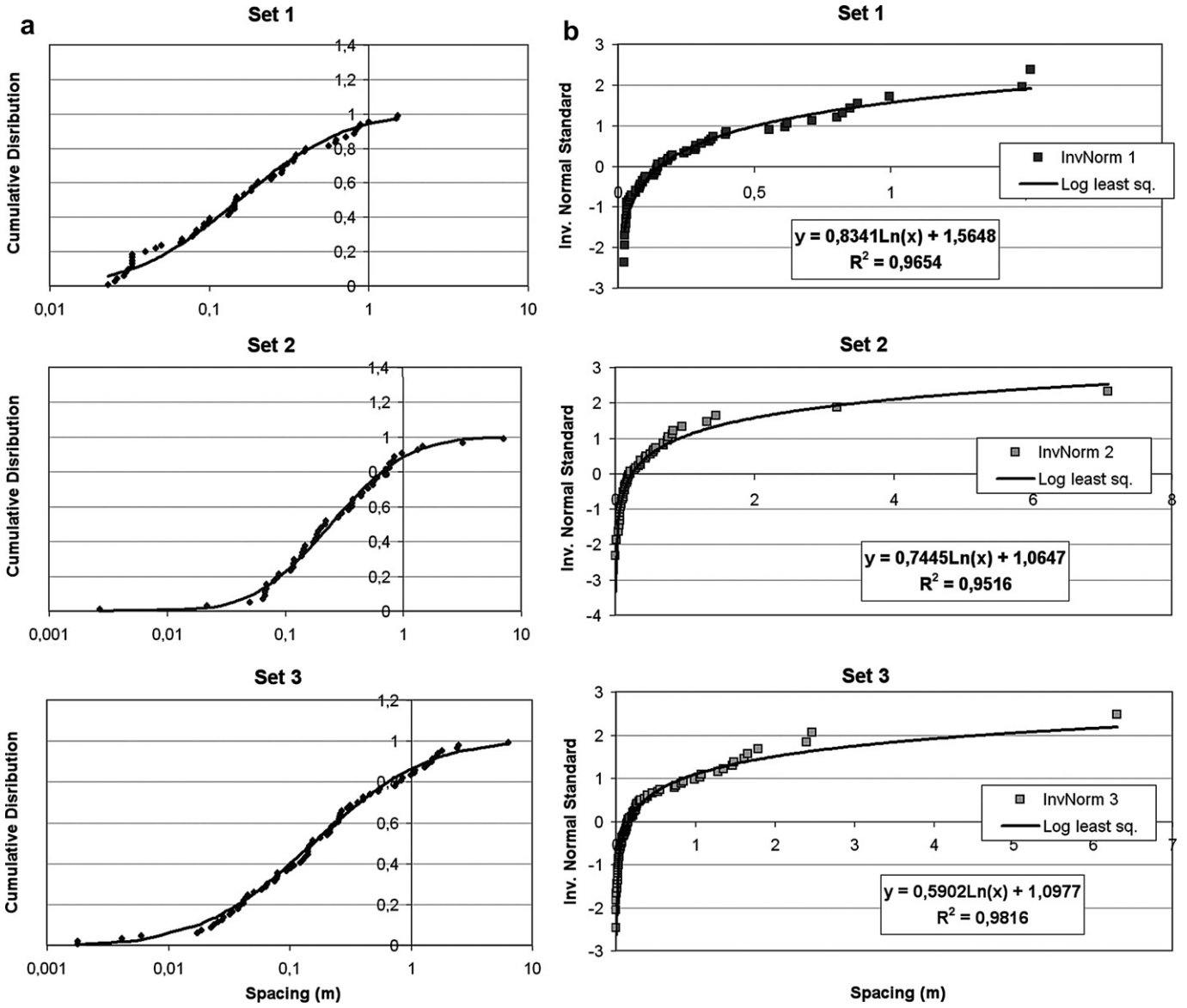

Fig. 10. Fracture analysis (scan-line data) for the main reactivated joint sets. (a) Cumulative frequency distribution of fracture spacing values. (b) Best-fit plots of the standard normal distribution inverse function of observed cumulative distributions vs. spacing. (c) Cumulative frequency distribution of fracture length values. (d) Best-fit plots of the standard normal distribution inverse function of observed cumulative distributions vs. length. (e) Semi-logarithmic plots of fracture length cumulative frequency, showing 90% confidence intervals and curves of normal, log-normal, and power-law distributions.

theoretical distribution best fitting the data. In case the data points are well aligned, the *AV* is a linear function of the standard normal *AV* and consequently is characterized by a Gaussian distribution. In our instance, the data points plot along a logarithmic curve, i.e. their distribution is well approximated by a linear function of $\ln(S)$. Therefore, $\ln(S)$ has a normal distribution (i.e. S is characterized by a log-normal distribution). By calculating the least squares curve on the semi-logarithmic diagram, a function is obtained of the type $u = a\ln(S) + b$ (shown in Fig. 10b), where u is the standard normal *AV*, while a and b are constants. Applying the standard Gaussian distribution function to the variable u, the log-normal distribution function is obtained as the best fit for the data points included in the diagrams of Fig. 10a. Mean fracture densities are of 3.47, 1.85, and 2.1 fractures m^{-1} for joint Sets 1, 2, and 3, respectively.

The analysis of joint length distributions (Fig. 10c and d) has been carried out with a method similar to that used for the analysis of fracture spacing. Also in this instance, the best-fit diagrams appear to outline a log-normal distribution. Such a distribution of fracture length values – as well as fracture spacing – has been observed in several studies where, however, normal and power-law distributions are also frequently reported (e.g. Gillespie et al., 1993; Odling et al., 1999). As for the evaluation of finite strain associated with joint reactivation we shall use the cumulative distribution function of fracture length (see Section 4.1), a more accurate statistical analysis concerning this parameter is relevant. Such an analysis is essentially devoted at defining whether fracture length data actually conform to a log-normal – rather than normal or power-law – distribution. To this purpose, in Fig. 10e the cumulative distributions of fracture length values are plotted for the three main reactivated joint sets, together with the 90% confidence intervals for each estimated cumulative frequency value (such intervals have been calculated by considering a uniform spatial distribution of joints, using the method outlined in Guerriero et al., in press). As it can be observed in the diagrams, the best-fit log-normal

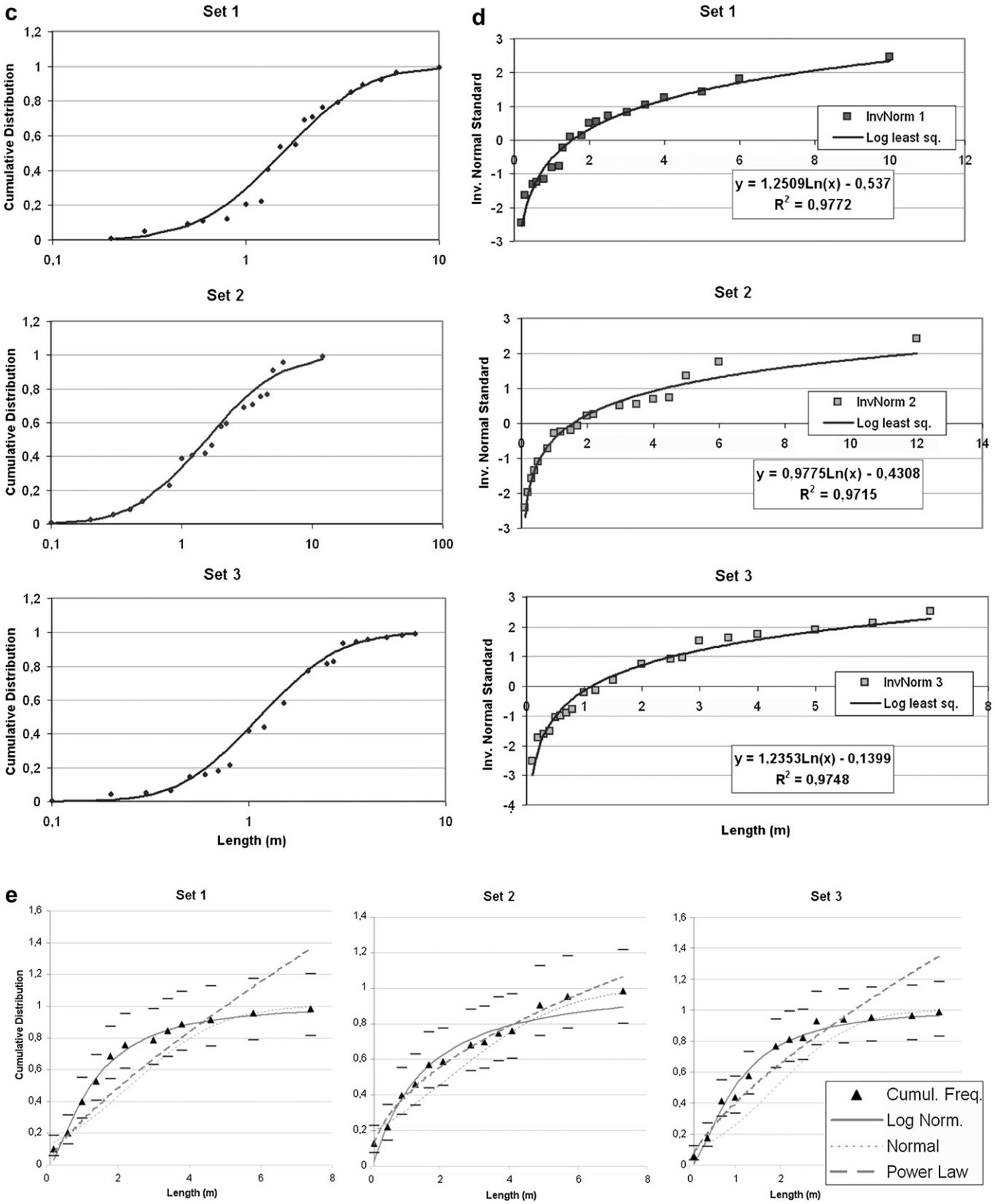

Fig. 10. (*continued*).

distribution – obtained using the best-fit diagrams of Fig. 10d by calculating the standard normal distribution of the least squares logarithmic function – is more consistently contained, with respect to both normal and power-law curves, within the confidence intervals of the cumulative frequency sampling estimates. Mean joint lengths are of 2.2, 2.65, and 1.7 m for joint Sets 1, 2, and 3, respectively.

4. Discussion

Tectonic inversion of the Eastern Cordillera Permo-Liassic rift system and shortening of the rift 'roots' produced widespread shear reactivation of primary joints within the Machu Picchu granitoid pluton. Analysis of fault slip data indicates that shear reactivation of different joint sets is kinematically consistent with ENE oriented shortening (Fig. 11). Therefore, although contractional deformation of the pluton may have resulted from a long history of tectonic inversion (Sempere et al., 2002), it appears that the shortening direction remained essentially constant during such a tectonic evolution. Lower greenschist facies metamorphic conditions during joint reactivation are indicated by the growth of chlorite, epidote and sericite, with a lack of higher-grade minerals. Such conditions are consistent with the microstructure of quartz observed in mylonitic shear zones, indicating dynamic recrystallization dominated by subgrain rotation recrystallization. The related deformation took place at depth, as the pluton was probably located toward the base of the upper crust. Therefore, it may be envisaged that most of the joint reactivation occurred during the early shortening stages, prior to the final ascent of the granitoid body as a result of strong inversion of the rift system. The lack of cataclastic overprinting of the more evolved, mylonitic shear zones suggests that slip along reactivated joints essentially ceased at shallower crustal levels, during pluton exhumation.

This work confirms that both brittle and mylonitic shear zones (Hull, 1988) can develop from precursor joints in plutonic rocks. In the study area, the transition from initial joints to faults, to mylonitic shear zones can be carefully documented. Shear zone types reflect the influence of fluid infiltration and the degree of fluid–rock interaction along the primary fracture. Fluid–rock interaction appears to have occurred along a great number of primary joints. However, both non-reactivated joints and brittle shear zones commonly display only limited (microscopically observable) wall-rock alteration by fluid–rock interaction. Mylonitic shear zones show a larger degree of fluid–rock interaction and substantial reaction softening. However, only <1% of observed shear zones (including both brittle and mylonitic types) consists of several tens of centimetres thick phyllonites. This, together with little wall-rock alteration and the lack of mineral-filled extension fractures and shear-related tension gashes, suggests minor dilatancy and limited fluid influx along precursor joints. This probably led to minor reaction softening and limited strain localization along individual ('weak') shear zones. Finite strain appears to have been mainly accommodated by a form of 'distributed shear' within the pluton, probably involving relatively small displacements accumulating over a very large number of primary fractures, which form a pervasive network at the batholith scale. Therefore, even though strain localization occurs at the metre scale, at the km (or pluton) scale strain can be considered as essentially distributed. This process of widespread reactivation of precursor joints is termed here 'diffuse faulting'.

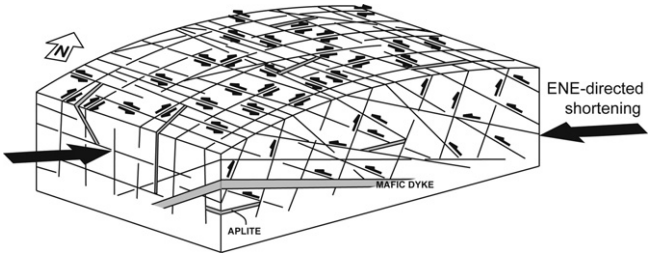

Fig. 11. Cartoon showing pluton deformation by widespread joint reactivation ('diffuse faulting'). Drawing of batholith fracture network was inspired by similar diagrams in Price and Cosgrove (1990), here adopted with orientation consistent with structures exposed in the Machu Picchu pluton.

4.1. How much strain at the pluton scale?

Faults and shear zones within the Machu Picchu pluton originated from reactivation of precursor fractures. Therefore, scan-line data analysis (Section 3.5) and related scaling relationships (Fig. 10) refer to structures that originated as joints. Numerous studies have shown that parameters such as aperture or length of tensional fractures display fracture-size relationships that are effectively described by log-normal or power-law distributions (e.g. Das Gupta, 1978; Mandelbrot, 1983; Nelson, 1985; Gudmundsson, 1987; Heffer and Bevan, 1990; Barton and Zoback, 1992; Gillespie et al., 1993; Sanderson et al., 1994; Barton, 1995; Gross and Engelder, 1995; Johnston and McCaffrey, 1996; Marrett, 1997; Odling et al., 1999; Ortega and Marrett, 2000; Ortega et al., 2006). On the other hand, joint spacing appears to be controlled by a series of parameters including (Nelson, 1985): (i) rock composition; (ii) rock texture, grain size, porosity; (iii) structural position; and (iv) mechanical layer thickness (a parameter that, in principle, should not apply to homogenous, roughly isotropic plutonic rocks, although early master joint sets are likely to control the development, in terms of size and spacing, of later joints).

The bulk finite strain associated with joint reactivation essentially results from the shear strain components produced by the three main reactivated joint Sets 1–3. In order to obtain the finite strain associated with each of the three main joint sets it would be necessary to know the statistic distribution $f(D)$ of displacements (D), that we define as the product between the probability density function (PDF) of D (e.g. Dekking et al., 2005) and mean fracture density (F_m): $f(D) = PDF(D) \cdot F_m$. The shear strain (γ) could then be obtained by the following integration:

$$\gamma = \int_0^\infty D \cdot f(D) \mathrm{d}D \tag{1}$$

where $f(D)\ \mathrm{d}D$ is the number of fractures per m having displacement comprised between D and $(D + \mathrm{d}D)$. In our instance, as a systematic measurement of displacements was hindered by the common lack of suitable markers, a statistically meaningful sample is unavailable. However, our field observations point out that displacements of few centimetres generally characterize fractures of metric size. Several studies (e.g. Cowie and Scholz, 1992; Schlische et al., 1996) unravelled a linear relationship between fault displacement (D) and fault length (L), the coefficient of proportionality being comprised between 10^{-3} and 10^{-1}. On the other hand, Wilkins et al. (2001) demonstrated that the D/L relationship appears to be rather weak in the case of reactivated joints, for which it is characterized by low values of the correlation coefficient. According to these Authors, since reactivated joints attain considerable length prior to slip, their D/L ratios are initially much smaller than those for primary faults. Furthermore, as magnitude of slip is not a consequence of fault growth, displacement across reactivated joints in certain cases may be independent of length.

Assuming that slip is independent of length, a constant value of slip (D^*) may be used for fractures having lengths larger than a threshold value (L_0) below which reactivation is supposed not to occur. In this case, the shear strain is given by:

$$\gamma = D^* \cdot \int_{L_0}^{\infty} f(L)\,\mathrm{d}L = D^* \cdot \int_{L_0}^{\infty} PDF(L) \cdot F_m\,\mathrm{d}L = D^* \cdot F(L_0) \qquad (2)$$

where f(L) dL is the number of fractures per m having length comprised between L and (L + dL), $F(L_0)$ is the product between the integral $\int_{L_0}^{\infty} PDF(L)\mathrm{d}L$ (given by $1 - CDF$, where CDF is the cumulative distribution of L_0; e.g. Dekking et al., 2005) and mean fracture density F_m, i.e. $F(L_0) = (1\text{-}CDF(L_0)) \cdot F_m$.

An alternative approach involves displacements varying as a function of length. It is worth noting that the data of Wilkins et al. (2001) on reactivated (stratabound) joints suggest a significant role of mechanical layering in controlling the dispersion of D/L ratios. In fact, stratabound – therefore constant-length – fractures contained within a single bed tend to accumulate a roughly constant displacement; however, different displacement values characterize stratabound fracture sets contained in beds of different thickness. Despite the control exerted by bedding, D/L ratios for the reactivated joints analyzed by Wilkins et al. (2001) are all in the range of $0.01 < D/L < 0.04$. As we are dealing with homogenous plutonic rocks for which there is no effect of mechanical layering, at a first approximation a linear relationship between D and L may be assumed in our variable displacement model. This would imply that: (i) larger fractures are able to accommodate larger displacements, and/or (ii) fracture growth occurred during joint reactivation. The relationship is of the type:

$$D = c \cdot L \qquad (3)$$

where c is a constant. In this instance, equation (1) takes the form:

$$\gamma = \int_{0}^{\infty} D \cdot f(L)\mathrm{d}L \qquad (4)$$

since a displacement $D = c \cdot L$ is associated with the number of fractures per m having length comprised between L and $L + dL$ (given by $f(L)$ dL). Therefore, equation (2) becomes:

$$\gamma = c \cdot \int_{0}^{\infty} L \cdot f(L)\mathrm{d}L = c \cdot \int_{0}^{\infty} L \cdot PDF(L) \cdot F_m \mathrm{d}L = c \cdot L^* \qquad (5)$$

where L^* represents the product between mean fracture length (given by: $\int_0^{\infty} L \cdot PDF(L)\mathrm{d}L$) and mean fracture density (F_m). Finite strain associated with joint reactivation may be tentatively evaluated using this constant aspect ratio (D/L) model, as well as the previous constant slip model. For the constant aspect ratio model, $c = 10^{-2}$ is assumed as a representative first-order approximation (Scholz, 1990). For the constant slip model, a value of $D = 3$ cm is assumed as a representative first-order approximation based on field observations (refer to Section 3.2); in this instance, a threshold length value of 1 m is used (i.e. it is assumed that joints of length below 1 m do not contribute to deformation at all). In both cases, the same constant aspect ratio and constant slip values are assumed for the three main reactivated joint sets. This seems a reasonable approximation taking into account that the three joint sets are at a similar angle (*ca.* 50°) with respect to the maximum compression direction associated with fracture reactivation. Finite strain calculations involve a series of steps described below.

For each joint set, the finite strain tensor is obtained using a reference frame having the x axis parallel to the slip vector, the z axis normal to fracture plane, and the y axis normal to both x and z. For the constant aspect ratio model, the strain tensors for joint Sets 1–3, obtained using equation (5), are:

$$T_1 = \begin{bmatrix} 1 & 0 & 0.08 \\ 0 & 1 & 0 \\ 0 & 0 & 1 \end{bmatrix}, \quad T_2 = \begin{bmatrix} 1 & 0 & 0.05 \\ 0 & 1 & 0 \\ 0 & 0 & 1 \end{bmatrix},$$
$$T_3 = \begin{bmatrix} 1 & 0 & 0.04 \\ 0 & 1 & 0 \\ 0 & 0 & 1 \end{bmatrix} \qquad (6)$$

whereas for the constant slip model the strain tensors for joint Sets 1–3, obtained using equation (2), are:

$$T_1 = \begin{bmatrix} 1 & 0 & 0.08 \\ 0 & 1 & 0 \\ 0 & 0 & 1 \end{bmatrix}, \quad T_2 = \begin{bmatrix} 1 & 0 & 0.04 \\ 0 & 1 & 0 \\ 0 & 0 & 1 \end{bmatrix},$$
$$T_3 = \begin{bmatrix} 1 & 0 & 0.04 \\ 0 & 1 & 0 \\ 0 & 0 & 1 \end{bmatrix} \qquad (7)$$

The strain tensors above are then referred to a common reference frame (arbitrarily chosen), and the composition of finite strain components is carried out for each model by multiplying the three matrices. As we are dealing with small finite strain values (of the order of few points percent), the order of matrix multiplication has a negligible effect.

For convenience – and obviously maintaining the concepts of strain and stress clearly distinct – a reference frame is adopted here whose axes lye parallel to the principal stress orientations determined by paleostress analysis (refer to Section 3.4). By referring the calculated finite strain to such a reference frame, the following tensors are obtained:

for the constant aspect ratio model,

$$T = \begin{bmatrix} 0.92 & -0.02 & 0.02 \\ -0.02 & 1.04 & 0.01 \\ -0.01 & 0.01 & 1.05 \end{bmatrix} \qquad (8)$$

whereas for the constant slip model,

$$T = \begin{bmatrix} 0.92 & -0.01 & 0.01 \\ -0.02 & 1.03 & 0.01 \\ -0.01 & 0.01 & 1.05 \end{bmatrix} \qquad (9)$$

Finally, orientation and magnitude of the principal finite strain axes may be obtained for the two cases of constant aspect ratio (Table 1) and constant slip (Table 2). The results are very similar for the two models. In both cases the finite strain ellipsoid is markedly oblate. The axis of maximum shortening (Z) is roughly horizontal and parallel to that of maximum compression (σ_1) determined by paleostress analysis. The finite strain tensors (8) and (9) also show that the bulk deformation resulting from reactivation of different joint sets is very close to coaxial, the non-diagonal components of the two matrices attaining very minor values. Considering an average pluton

Table 1
Parameters of the finite strain ellipsoid obtained by the constant aspect ratio (D/L) model (see text).

	X; $(1+e_1)$	Y; $(1+e_2)$	Z; $(1+e_3)$
Trend	346	162	254
Plunge	40	50	2
$(1+e)$	1.054	1.033	0.920

Table 2
Parameters of the finite strain ellipsoid obtained by the constant slip model (see text).

	X; $(1+e_1)$	Y; $(1+e_2)$	Z; $(1+e_3)$
Trend	347	162	254
Plunge	51	39	2
$(1+e)$	1.053	1.032	0.920

diameter of *ca*. 30 km (Carlotto et al., 1996), the finite strain values obtained by both models would result in *ca*. 2.5 km of horizontal shortening across the granitoid body. Of course this value represents just a first-order approximation, as it depends on the input parameters of fracture displacement and the assumptions on D/L relationships for reactivated joints. In this study, a conservative approach has been chosen in the evaluation of bulk finite strain. For instance, the contribution of slip along fractures not belonging to the main joint Sets 1–3 has been neglected. For the constant slip model, the contribution to deformation by fractures having length <1 m has also been neglected. Furthermore, larger displacements likely associated with mylonitic shear zones have not been taken into account. Considering the rather subordinate occurrence of ductile shear zones (and even more rare phyllonites), as well as the likely amounts of displacements associated with tens of centimetres thick ductile shear zones (being of the order of the tens of metres according to Hull, 1988), the contribution of mylonitic shear zones to bulk finite strain at the pluton scale is likely to be minor. Nevertheless, our modelling most probably yields minimum finite strain estimates. Yet these are likely to represent reasonable approximations for bulk pluton deformation in terms of: (i) order of magnitude of finite strains; (ii) principal finite strain axes orientation; (iii) reciprocal proportions of principal finite strain axes magnitudes; and (iv) proportions of coaxial vs. non-coaxial strain components.

5. Concluding remarks

- The Machu Picchu pluton displays different stages of shear zone evolution, from (dominant) fault-like reactivation of primary joints to (subordinate) mylonitic shear zone development – with rare formation of more retrogressed phyllonites – apparently reflecting the influence of fluid influx along precursor fractures.
- Paleostress analysis indicates that shear reactivation of different joint sets is kinematically consistent with ENE oriented shortening associated with tectonic inversion of the Permo-Liassic rift system in the high Eastern Cordillera.
- Deformation was accommodated by a form of distributed shear – here termed 'diffuse faulting' – probably involving relatively small displacements occurring over a very large number of primary fractures, which form a pervasive network within the pluton. Therefore, although strain localization occurs at the metre scale, at the kilometre (or pluton) scale strain is essentially distributed.
- Theoretical modelling based on fracture analysis and on the application of various displacement–length relationships suggests that reactivation of different master joint sets resulted in pluton deformation dominated by markedly oblate, bulk coaxial strain.
- Our modelling suggests that the process of 'diffuse faulting' is likely to have accommodated relatively limited finite strains in terms of percent shortening (8% according to our conservative estimates); yet, this yields a significant crustal shortening (of a few kilometres) when deformation is integrated across the whole granitoid body.

Acknowledgments

The paper greatly benefited from thoughtful and constructive critical comments by JSG Reviewer Fernando Hongn and Editor Joao Hippertt. *ISPRA* co-authors of this paper gratefully acknowledge the financial support from their institution (formerly ENEA). ISPRA co-authors carried out the present activities under the project INTERFRASI, funded by the Italian Ministry of University and Scientific Research and coordinated by Paolo Canuti and Claudio Margottini. Field activities greatly benefited from the support of the Instituto Nacional de Cultura (INC) in Machu Picchu, for which the Director Ferdinando Astete is thanked sincerely.

References

Angelier, J., Mechler, P., 1977. Sur une méthode graphique de recherché des contraintes principales également utilisable en tectonique et en séismologie: la méthode des dièdres droits. Bulletin de la Société Géologique de France 19, 1309–1318.
Barton, C.A., Zoback, M.D., 1992. Self-similar distribution and properties of macroscopic fractures at depth in crystalline rock in the Cajon Pass Scientific Drill Hole. Journal of Geophysical Research 97, 5181–5200.
Barton, C.C., 1995. Fractal analysis of scaling and spatial clustering of fractures. In: Barton, C.C., La Pointe, P.R. (Eds.), Fractals in the Earth Sciences. Plenum Press, pp. 141–178.
Buchanan, J.G., Buchanan, P.G. (Eds.), 1995. Basin Inversion. Geological Society of London Special Publication 88.
Butler, R.W.H., Mazzoli, S., 2006. Styles of continental contraction: a review and introduction. In: Mazzoli, S., Butler, R.W.H. (Eds.), Styles of Continental Contraction. Geological Society of America, Special Paper 414, pp. 1–10. doi:10.1130/2006.2414(01).
Carlotto, V., 2002. Evolution andine et raccourcissement au niveau de Cusco (13–16°S) Pérou. Thèse de Doctorat Université Joseph Fourier, Grenoble, Géologie Alpine, Mémoire Hors Série 39, p. 203.
Carlotto, V., Gil, W., Cardenas, J., Chàvez, R., 1996. Geologìa de los cuadrangulos de Urubamba y Calca hojas 27-r y 27-s. Boletin INGEMMET, sèrie A, Carta Geologica Nacional 65.
Cooper, M.A., Williams, G.D. (Eds.), 1993. Inversion Tectonics. Geological Society Special Publication 44.
Cowie, P.A., Scholz, C.H., 1992. Displacement–length scaling for faults: data synthesis and discussion. Journal of Structural Geology 14, 1149–1156.
Christiansen, P.P., Pollard, D.D., 1997. Nucleation, growth and structural development of mylonitic shear zones in granitic rock. Journal of Structural Geology 19, 1159–1172.
Dekking, F.M., Kraaikamp, C., Lopuhaa, H.P., Meester, L.E., 2005. A Modern Introduction to Probability and Statistics: Understanding Why and How. Springer-Verlag, London.
Das Gupta, U., 1978. A Study of Fractured Reservoir Rocks, with Special Reference to Mississippian Carbonate Rocks of Southwest Alberta. Ph.D. thesis, University of Toronto.
Gillespie, P.A., Howard, C.B., Walsh, J.J., Watterson, J., 1993. Measurement and characterization of spatial distributions of fractures. Tectonophysics 226, 113–141.
Glen, R.A., Hancock, P.L., Whittaker, A., 2005. Basin inversion by distributed deformation: the southern margin of the Bristol Channel Basin, England. Journal of Structural Geology 27, 2113–2134.
Gross, M.R., Engelder, T., 1995. Strain accommodated by brittle failure in adjacent units of the Monterey Formation, U.S.A.: scale effects and evidence for uniform displacement boundary conditions. Journal of Structural Geology 17, 1303–1318.
Gudmundsson, A., 1987. Geometry, formation, and development of tectonic fractures on the Reykjanes Peninsula, southwest Iceland. Tectonophysics 139, 295–308.
Guerriero, V., Iannace, A., Mazzoli, S., Parente, M., Vitale, S., Giorgioni, M. Quantifying uncertainties in multi-scale studies of fractured reservoir analogues: implemented statistical analysis of scan line data. Journal of Structural Geology, in press, doi: 10.1016/j.jsg.2009.04.016.
Heffer, K.J., Bevan, T.G., 1990. Scaling relationships and natural fractures: data, theory and applications. In: Society of Petroleum Engineers, Europec 90, The Hague, October 22–24, SPE Paper 209819, 367–376.
Hull, J., 1988. Thickness–displacement relationships for deformation zones. Journal of Structural Geology 10, 431–435.
Jaillard, E., Herail, G., Monfret, T., Worner, T., 2002. Andean geodynamics: main issues and contributions from the 4th ISAG, Gottingen. Tectonophysics 345, 1–15.

Johnston, J.D., McCaffrey, K.J.W., 1996. Fractal geometries of vein systems and the variation of scaling relationships with mechanism. Journal of Structural Geology 18, 349–358.
Lancelot, J.R., Laubacher, G., Marocco, R., Renaud, U., 1978. U/Pb radiochronology of two granitic plutons from the Eastern Cordillera (Peru): extent of Permian magmatic activity and consequences. Geologische Rundschau 67, 236–243.
Mancktelow, N.S., Pennacchioni, G., 2005. The control of precursor brittle fracture and fluid–rock interaction on the development of single and paired ductile shear zones. Journal of Structural Geology 27, 645–661.
Mandelbrot, B., 1983. The Fractal Geometry of Nature. Freeman and Company, New York.
Marrett, R., 1997. Permeability, porosity, and shear-wave anisotropy from scaling of open fracture populations. In: Hoak, T.E., Klawitter, A.L., Blomquist, P.K. (Eds.), Fractured Reservoirs: Characterization and Modeling Guidebook. Rocky Mountain Association of Geologists, pp. 217–226.
Nelson, R.A., 1985. Geologic Analysis of Naturally Fractured Reservoirs. Gulf Publishing, Houston.
Odling, N.E., Gillespie, P., Bourgine, B., Castaing, C., Chiles, J.P., Christensen, N.P., Fillion, E., Genter, A., Olsen, C., Thrane, L., Trice, R., Aarseth, E., Walsh, J.J., Watterson, J., 1999. Variations in fracture system geometry and their implications for fluid flow in fractured hydrocarbon reservoirs. Petroleum Geoscience 5, 373–384.
Ortega, O., Marrett, R., 2000. Prediction of macrofracture properties using microfracture information, Mesaverde Group sandstones, San Juan basin, New Mexico. Journal of Structural Geology 22, 571–588.
Ortega, O., Marrett, R., Laubach, E., 2006. Scale-independent approach to fracture intensity and average spacing measurement. AAPG Bulletin 90, 193–208.
Pennacchioni, G., 2005. Control of the geometry of precursor brittle structures on the type of ductile shear zone in the Adamello tonalites, Southern Alps (Italy). Journal of Structural Geology 27, 627–644.
Pennacchioni, G., Mancktelow, N.S., 2007. Nucleation and initial growth of a shear zone network within compositionally and structurally heterogeneous granitoids under amphibolite facies conditions. Journal of Structural Geology 29, 1757–1780. doi:10.1016/j.jsg.2007.06.002.
Price, N.J., Cosgrove, J.W., 1990. Analysis of Geological Structures. University Press, Cambridge.
Ramos, V.A., Aleman, A., 2000. Tectonic evolution of the Andes. In: Cordani, U.G., et al., (Eds.), Tectonic Evolution of South America, 31st International Geological Congress, Rio de Janeiro, 635–685.
Ramsay, J.G., Graham, R.H., 1970. Strain variation in shear belts. Canadian Journal of Earth Sciences 7, 786–813.
Sanderson, D.J., Roberts, S., Gumiel, P., 1994. A fractal relationship between vein thickness and gold grade in drill core from La Codosera, Spain. Economic Geology 89, 168–173.
Schlische, R.W., Young, S.S., Ackermann, R.V., Gupta, A., 1996. Geometry and scaling relations of a population of very small rift-related normal faults. Geology 24, 683–686.
Scholz, C.H., 1990. Mechanics of Earthquakes and Faulting. Cambridge University Press.
Sempere, T., Carlier, G., Soler, P., Fornari, M., Carlotto, V., Jacay, J., Arispe, O., Neraudeau, D., Cardenas, J., Rosas, S., Jimenez, N., 2002. Late Permian–Middle Jurassic lithospheric thinning in Peru and Bolivia, and its bearing on Andean-age tectonics. Tectonophysics 345, 153–181.
Tourigny, G., Tremblay, A., 1997. Origin and incremental evolution of brittle/ductile shear zones in granitic rocks: natural examples from the southern Abitibi Belt, Canada. Journal of Structural Geology 19, 15–27.
Turner, F.J., 1953. Nature and dynamic interpretation of deformation lamellae in calcite of three marbles. American Journal of Science 251, 276–298.
Vitale, S., Mazzoli, S., 2008. Heterogeneous shear zone evolution: the role of shear strain hardening/softening. Journal of Structural Geology 30, 1383–1395. doi:10.1016/j.jsg.2008.07.006.
Vitale, S., Mazzoli, S., 2009. Finite strain analysis of a natural ductile shear zone in limestones: insights into 3-D coaxial vs. non-coaxial deformation partitioning. Journal of Structural Geology 31, 104–113. doi:10.1016/j.jsg.2008.10.011.
Wallbrecher, E., 1986. Tektonische und Gefügeanalytische Arbeitsweisen. Enke-Verlag, Stuttgart.
Wilkins, S.J., Gross, M.R., Wacker, M., Eyal, Y., Engelder, T., 2001. Faulted joints: kinematics, displacement–length scaling relations and criteria for their identification. Journal of Structural Geology 23, 315–327.